Aalborg Universitet

AALBORG UNIVERSITY

Investigation of Multi-Step Fast Charging Protocol and Aging Mechanism for Commercial NMC/Graphite Lithium-ion Batteries

Li, Yaqi; Guo, Jia; Pedersen, Kjeld; Gurevich, Leonid; Stroe, Daniel-Ioan

Published in:
Journal of Energy Chemistry

DOI (link to publication from Publisher):
10.1016/j.jechem.2023.01.016

Creative Commons License
CC BY 4.0

Publication date:
2023

Document Version
Publisher's PDF, also known as Version of record

Link to publication from Aalborg University

Citation for published version (APA):
Li, Y., Guo, J., Pedersen, K., Gurevich, L., & Stroe, D.-I. (2023). Investigation of Multi-Step Fast Charging Protocol and Aging Mechanism for Commercial NMC/Graphite Lithium-ion Batteries. *Journal of Energy Chemistry*, *80*, 237-246. https://doi.org/10.1016/j.jechem.2023.01.016

General rights
Copyright and moral rights for the publications made accessible in the public portal are retained by the authors and/or other copyright owners and it is a condition of accessing publications that users recognise and abide by the legal requirements associated with these rights.

- Users may download and print one copy of any publication from the public portal for the purpose of private study or research.
- You may not further distribute the material or use it for any profit-making activity or commercial gain
- You may freely distribute the URL identifying the publication in the public portal -

Take down policy
If you believe that this document breaches copyright please contact us at vbn@aub.aau.dk providing details, and we will remove access to the work immediately and investigate your claim.

Downloaded from vbn.aau.dk on: December 05, 2025

Journal of Energy Chemistry 80 (2023) 237–246

Contents lists available at ScienceDirect

Journal of Energy Chemistry

journal homepage: www.elsevier.com/locate/jechem

http://www.journals.elsevier.com/journal-of-energy-chemistry/

Investigation of multi-step fast charging protocol and aging mechanism for commercial NMC/graphite lithium-ion batteries

Yaqi Li [a,b], Jia Guo [a,b,*], Kjeld Pedersen [a], Leonid Gurevich [a], Daniel-Ioan Stroe [b]

[a] Department of Materials and Production, Aalborg University, Aalborg 9220, Denmark
[b] Department of Energy, Aalborg University, Aalborg 9220, Denmark

ARTICLE INFO

Article history:
Received 21 November 2022
Revised 29 December 2022
Accepted 12 January 2023
Available online 24 January 2023

Keywords:
Fast-charging
Lithium-ion battery
Aging mechanism
Electrode

ABSTRACT

Fast charging is considered a promising protocol for raising the charging efficiency of electric vehicles. However, high currents applied to Lithium-ion (Li-ion) batteries inevitably accelerate the degradation and shorten their lifetime. This work designs a multi-step fast-charging method to extend the lifetime of $LiNi_{0.5}Co_{0.2}Mn_{0.3}O_2$ (NMC)/graphite Li-ion batteries based on the studies of half cells and investigates the aging mechanisms for different charging methods. The degradation has been studied from both full cell behaviour and materials perspectives through a combination of non-destructive diagnostic methods and post-mortem analysis. In the proposed multi-step charging protocol, the state-of-charge (SOC) profile is subdivided into five ranges, and the charging current is set differently for different SOC ranges. One of the designed multi-step fast charging protocols is shown to allow for a 200 full equivalent cycles longer lifetime as compared to the standard charging method, while the charging time is reduced by 20%. From the incremental capacity analysis and electrical impedance spectroscopy, the loss of active materials and lithium inventory on the electrodes, as well as an increase in internal resistance for the designed multi-step constant-current-constant-voltage (MCCCV) protocol have been found to be significantly lower than for the standard charging method. Post-mortem analysis shows that cells aged by the designed MCCCV fast charging protocol exhibit less graphite exfoliation and crystallization damage, as well as a reduced solid electrolyte interphase (SEI) layer growth on the anode, leading to a lower R_{sei} resistance and extended lifetime.

© 2023 Science Press and Dalian Institute of Chemical Physics, Chinese Academy of Sciences. Published by ELSEVIER B.V. and Science Press. This is an open access article under the CC BY license (http://creativecommons.org/licenses/by/4.0/).

1. Introduction

In recent years, lithium-ion (Li-ion) batteries have become the most popular energy storage solution in modern society, especially for powering battery electric vehicles (BEVs). However, there are also some unmet needs when using Li-ion batteries in BEV applications, such as the limited range, slow charging etc. Fast charging of Li-ion batteries can help to reduce the range anxiety and improve the overall acceptance of electric vehicles. However, fast charging may also accelerate battery degradation due to solid electrolyte interphase (SEI) formation and exfoliation on the anode [1–3]. This is because fast charging typically involves high charging current rates and high temperatures, which are the main factors in SEI formation [4,5]. Various factors may affect the capability of a Li-ion cell to achieve and withstand fast charging conditions, including properties of the active electrode materials, cell level design, and fast charging strategies [6,7]. Most previous studies focused on electrode active materials and battery cell level design to improve fast charging performance [8–10]. On the other hand, the effect of different fast-charging protocol on battery degradation remains largely unknown. In this work we attempt to approach systematically the effect of the number of fast charging steps, C-rates, and state-of-charge (SOC) ranges/steps on battery degradation and charging time to meet both the requirements of extending the lifetime and the efficiency.

To perform fast charging, a time-dependent charging current profile is a necessity to reduce battery degradation. In the standard constant-current constant-voltage (CCCV) charging protocol, the cell is charged at a constant current level until the cell voltage reaches a predetermined upper limit. Although this protocol simplifies the design of battery chargers, it is not suitable for fast charging, as constant charging at high C-rates increases the degradation rate and has a negative impact on the battery lifetime [11,12]. This can be improved by using a charging current profile varying as a function of SOC. An important advantage of this

* Corresponding author.
E-mail address: jgu@energy.aau.dk (J. Guo).

https://doi.org/10.1016/j.jechem.2023.01.016
2095-4956/© 2023 Science Press and Dalian Institute of Chemical Physics, Chinese Academy of Sciences. Published by ELSEVIER B.V. and Science Press.
This is an open access article under the CC BY license (http://creativecommons.org/licenses/by/4.0/).

approach is that it does not require changes in battery production technology and can applied immediately to the batteries already in use.

Fast charging has been investigated in recent years. There have been many discussions about the difficulties and potential paths for future research into fast charging at the level of battery materials from the perspectives of mass transportation, charge transfer, and thermal management, as well as the requirements and optimization tactics for the electrode, electrolyte, and electrode/electrolyte interface [4,13]. The progress on electrolytes for fast charging is also discussed, traditional electrolytes are unable to enable fast charging. Advanced fast-charging electrolytes can be created by modifying the structure and stability of the Li^+ solvation shell using various solvents, lithium salts, and electrolyte additives [14]. Metal anode has also been employed for enabling fast charging, e.g., a newly created Li-based metal–organic framework (Li-MOF) coating is used to govern ion transportation via a functional polypropylene (PP) separator [15]. Meanwhile, instead of changing the material/electrolyte to fully harvest benefits of fast charging but adjusting the charging protocols can reduce the charging time, which is cheap and simple and can be applied to existing batteries. Several fast-charging protocols have also been proposed in literature, but their effect on electrode degradation is rarely reported [16–18]. For instance, health-conscious fast charging protocols have been designed using degradation models to reduce the charge time as well as the battery degradation; the work shows the potential of optimized charging strategies in reducing the charge duration and battery degradation [19,20]. A two-step fast charging protocol was also be proposed, and the simulation results indicate that their protocol can achieve a lower capacity fade ratio [21].

In this work, a multi-step fast-charging protocol is designed based on the measurements of a graphite/Li coin cell and applied to commercial cylindrical NMC/graphite cells. Eight cells were aged under multi-step fast charging and standard CCCV charging, and the cells under the MCCCV charging method were found to show the longest lifetime. The aging mechanisms associated with different charging methods were studied by non-destructive techniques as well as post-mortem analysis. The methodology combined in-situ and ex-situ methods to investigate the influence of different charging methods on the aging mechanism at the full cell, electrode, and material levels. After reaching 10% capacity fade, one cell per test case was disassembled in a glove box, and morphology, composition, and structure of electrodes were studied to explain the aging mechanisms.

The paper is organized as follows: Section 2 describes the idea behind the protocols for the coin cell tests, and the designed test matrix for cylindrical cells. Section 3 shows the design of the multi-step fast charging method and discusses the changes in the cells' electrical parameters to explain the aging mechanism. Section 4 presents a detailed investigation of the aging mechanism at the electrode and material levels. Section 5 is a conclusion.

2. Experimental

2.1. Coin cell measurements

Coin cell tests for evaluating the incremental capacity of graphite electrode were performed. Graphite anodes were obtained from freshly disassembled 18,650 cylindrical full cells (Samsung, INR18650-20R, 2 A h, 2.5–4.2 V, Max. charge current 4 A), then cut into 14 mm-diameter discs, paired with 15 mm-diameter-lithium metal discs and assembled into CR2016-coin cell cases. The electrolyte was 1 M $LiPF_6$ in dimethyl carbonate (DMC)/diethyl carbonate (DEC) mixed in a 1:1 ratio. The graphite/Li coin cells were repeatedly charged and discharged with a Landt coin cell tester (CT 2001A, Landt, China), using a constant current of 0.8 mA which is equivalent to 0.2 C-rate (such coin cells showed a typical capacity of 3.8 mA h).

2.2. Full cell measurements

Full cell testing was carried out on commercially available 18,650 cylindrical cells (Samsung) with a capacity of 2 A h and a nominal voltage of 3.6 V. The cells employ $LiNi_{0.5}Co_{0.2}Mn_{0.3}O_2$ and synthetic graphite as cathode and anode materials, respectively. Eight cells were tested using a Neware battery test station (5V12A, Neware, China) following four different aging cycles, as summarized in Table 1. The corresponding charge time for the protocols is shown in Table S1. The design idea of the test matrix is discussed in Section 3. Two cells were used for every test. The test program is shown in Fig. S1.

For the aging test, the entire SOC interval was divided into five stages of 20% SOC, each with different constant charging currents. The highest C-rates possible for the commercial NMC cell used is 2 C as specified in the manufacturer's datasheet. The C-rates were reduced to 1.5, 1, and 0.5 C after each 20% SOC stage. The constant voltage charging method was used after the voltage reached 4.2 V, the charging continued until the current dropped to 0.1 A. In the MCCCV charging process, the charging time of a 2 A h full cell to 80% SOC was under 30 min. For comparison, the standard constant-current-constant-voltage (CCCV) protocol was used for other two sets of batteries from the same batch with 1 and 2 C constant current charging, respectively. Discharging was done using the same WLTC driving cycle in all four cases. All the tests were carried out in a thermostatic enclosure at 25 °C.

Reference performance test (RPT): After every 100 full equivalent cycles (FEC) of the above fast-charging protocols, RPT at 25 °C were conducted to investigate and quantify the degradation of the cells. To measure the capacity, the cells were charged at a 0.5 C rate (i.e., 1 A) to 4.2 V using a CC-CV profile; the cells were considered fully charged when the cut-off current reached a value of 0.1 A. Then, after a 15-min delay, the cells were discharged to 2.5 V with a continuous current of 0.5 C. The impedance spectra of the cells were measured with a Digatron EIS analyzer in a frequency range of 6.5 kHz to 10 mHz. A suitable equivalent circuit model was used to fit the measured EIS spectra using ZView (Scribner Associates), as shown in Section 3.

2.3. Post-mortem characterization

After the cells reached 10% capacity fade, they were fully discharged, transferred into a glove box with an argon atmosphere and disassembled. Afterwards, the electrodes were thoroughly rinsed three times with DEC and immediately transferred for subsequent characterization. The morphology of graphite anodes was visualized using a Scanning Electron Microscope (Zeiss XB1540, Carl Zeiss) operating at 20 keV. X-ray diffraction (Empyrean, Panalytical) was performed to measure the graphite anode structure at 45 kV with a scanning speed of 2°/min. The damage to graphite crystallinity was also characterized with Raman Spectroscopy (Invia Micro-Raman spectroscope, Renishaw). Differential Scanning Calorimetry (Q2000, TA Instruments) was used to test the thermal stability. The composition of the electrode surfaces was analyzed by an X-ray Photoelectron Spectrometer (XPS, Phoibos 150 1D-DLD, XR 50, Specs).

3. Design and electrical performance of multi-step fast charging protocols

From the previous work on the degradation of NMC/graphite batteries, it was concluded that the anode decay is always the

Table 1
Test matrix with four charging protocols.

SOC stages	0–20%	20%–40%	40%–60%	60%–80%	80%–100%
1 C	1 C CCCV standard charge				
2 C	2 C CCCV fast charge				
MCCCV1	2 C	2 C	1.5 C	1 C	0.5 C/CV
MCCCV2	2 C	1.5 C	1.5 C	1 C	0.5 C/CV

dominant process contributing to the capacity fade [22–24]. Here, the graphite anode was retrieved from fresh commercial cylindrical cells to build coin cells, with an aim to analyze the graphite electrochemical behavior during cycling. Li-metal was used as the counter electrode in the coin cells, which were tested at 0.2 C, as mentioned in Section 2.1. Fig. 1(a) presents the electrochemical behavior of graphite coin cell at 0.2 C. The blue line represents de-lithiation on graphite, which corresponds to the discharge process in a full cell; the red line is the lithiation of graphite which represents the charging process in a full cell. The capacity for all coin cells was about 3.8 mA h. In the charge range of 0–0.76 mA h, which corresponds to 0–20% SOC, the voltage changes fast, which indicates that the first 20% lithiation experienced a wide voltage range.

The incremental capacity analysis (IC) was also employed to confirm the process of capacity change. As shown in Fig. 1(b), the voltage range is the largest at the beginning of the charging process, corresponding to 0% to 20% SOC. As the SOC becomes higher, between 20–40%, the voltage increase becomes to almost one-fourth of the first 20% SOC. The evident graphite characteristic peaks at different SOC conditions can be seen in all XRD patterns at roughly 27° in Fig. 1(c), and these peaks move with the evolution of the voltage. The crystal plane of the anode will change from different SOC, and at 140 mV (20% SOC) exhibited the similar phase to the fully discharged anode (260 mV). However, as the voltage of the anode decrease, which means the SOC of the full cell increase, the d-spacing is also enlarging. Comparing to the *d*-spacing of 3.34 Å for pure graphite, as the lithiation from 260 mV to 0 mV, the d-spacing increases gradually from 3.43 to 3.65 Å. Increasing the current intensity during the phase change process leads to a subsequent increase in mechanical stress, resulting in the breakage of the graphite particles. At the same time, the increase in d-spacing leads to the rupture of the SEI film, which in turn increases the resistance [25]. Moreover, the phase transition in graphite anode is observed at around 25% lithiation, which indicates that substantial strain in the lattice [26]. A multi-step fast-charging protocol is introduced to efficiently utilize the charging time and protect the lifetime of the batteries. The proposed test matrix is shown in Table 1 in Section 2. The charging profile is shown in Fig. 2(a), which exhibits the current change in the MCCCV2 charging protocol. The World Harmonized Light Vehicles Test Cycle (WLTC) driving cycle was used as the discharge profile to simulate real driving conditions and applied five consecutive times to fully discharge the cells. Note that the WLTC is designed to be similar to actual discharge cycle experienced by a battery on an electric car. Acceleration and deceleration in the WLTC are not periodic, which better reflects the motion of a car on roads with different degrees of congestion and rolling resistance; gear change, vehicle weight and other factors of real driving conditions are also taken into account in the test.

All batteries underwent reference performance testing (RPT), which included capacity and EIS tests, after every 100 full equivalent cycles (FEC). For EVs, the end-of-life capacity for battery is set to 80%, and improper fast charging protocols may lead to capacity fading acceleration [11,27]. Here, two batteries are used for each test case. One battery of each test cases is disassembled at 90% capacity fade, while the other one is opened at the end-of-life (20%) capacity fade. This manuscript analyses the four test cases with 10% degradation, aiming to explain how the charge current influences the performance on both macro and micro level and whether varying the charging current as a function of the SOC can extend the battery lifetime. The capacity fade behavior in the first 10%, expressed as state of health (SOH), of the cells aged using the four conditions, is presented in Fig. 2(b). In the first 100 cycles of the aging process, the cells aged using 1 and 2 C constant charging currents, as well as MCCCV1 charging profile exhibited a reduction in capacity with a greater slope, culminating in a 2% capacity fade, as opposed to the just 1% capacity fade when MCCCV2 was used. The cells aged under CCCV and MCCCV1 showed a rapid capacity fade, reaching 10% capacity fade after 500 FEC. On the other hand, when MCCCV2 charging profile was used, the cells could perform 200 additional FEC before reaching the same degradation level. Low charging current (0.5 C) applied when the battery was charged over 80% SOC and a lower current between 20%–40% SOC are thought to play a significant role in the slower capacity decline. As lithiation speeds up at a higher SOC, a higher charging current leads to a degradation of the graphite anode, and cracks and exfoliation cause the anode to collapse, resulting in a capacity fade. On the other hand, excessive charging currents at 20%–40% SOC also lead to capacity fade according to the XRD results in Fig. 1(c), when the lithium ion inserted into graphite, the crystallization will change when the SOC reaches 20%. Higher current leads to large mechanical stress, which can damage the anode as well as lead to the loss of active materials. An increase in the interlayer spacing in graphite also leads to rupture of the SEI film, which increases the battery electrical resistance. It is worth noting that

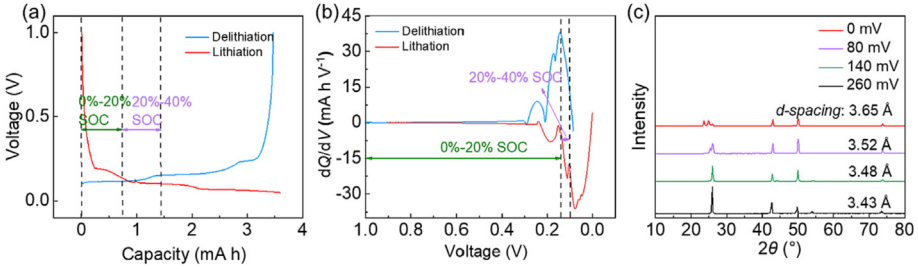

Fig. 1. Charge-discharge curve (a) of graphite/Li coin cells and corresponding IC curve (b); (c) ex-situ XRD patterns for the structure evolution during lithiation of graphite in a graphite/Li half-cell.

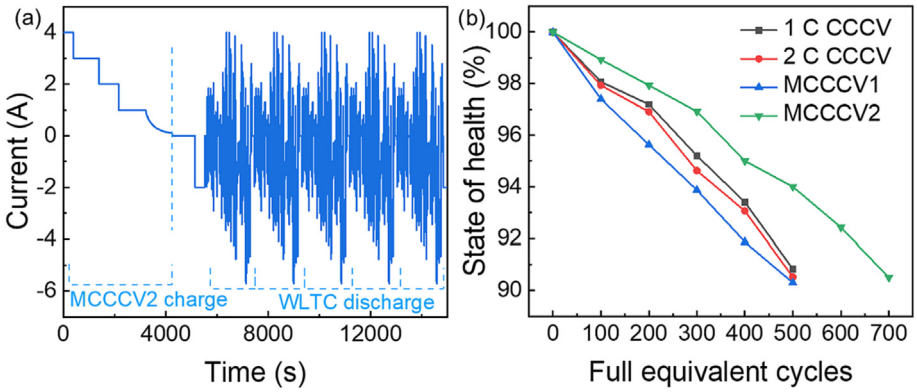

Fig. 2. The detailed MCCCV2 current charging profile (a) and state-of-health (b) conditions after 10% capacity fade for 18,650 NMC/graphite cells.

for the 2 C test cases, 2 C-CCCV charge method is provided, which means the battery will reach 4.2 V earlier than the MCCCV1 according to Table S1 in the revised paper, therefore, a longer CV step was used in the 2 C-CCCV protocol than MCCCV1. Compared to CC charge, CV charge can minimize the damage to the electrodes as much as possible, due to the decreasing charging current during the charging process. As a result, it leads to the phenomenon that the state of health (SOH) of MCCCV1 is instead less than the conventional high-current (2 C) charging scheme.

The charging-discharging voltage curves measured every 100 FEC and the corresponding IC curves are shown in Fig. 3. In the IC curves, the intensity of the main peak around 3.7 V decreases with the number of FEC in all the cases. This behavior is related to the loss of active materials in the positive electrode or negative electrode [28]. For an IC curve, the main peak intensity represents the amounts of active materials, while the height of the second most intense peak is related to available graphite in the anode [29–31]. As the intensity of the peak decreases, the internal resistance is increased. MCCCV2 protocol shows the least increase in internal resistance, as well as the minimal loss of active materials. In contrast, the two CCCV charging protocols studied exhibited the most pronounced drop in the intensity of the secondary peak between begin-of-life and after 500 FEC. This proves that the proposed multi-step charge method is suitable for protecting batteries from fast degradation as will be further demonstrated by post-mortem analysis in Section 4.

The EIS technique was used to analyze the aging mechanisms of the tested cells. The evolution of the impedance spectra of the cells aged under the four considered conditions and the comparison of the four conditions at 500 FEC are illustrated in Fig. 4(a–e). In the high- and medium-frequency ranges, the two semicircles represent the total interfacial resistance from the solid electrolyte interphase (SEI, R_{sei}) and the charge transfer resistance (R_{ct}), respectively [32]. The measured impedance spectra were fitted using the equivalent circuit shown in Fig. 4(f). The fitting results indicate an increase in the thickness of SEI layer in all four test scenarios. Capacity fading is also caused by the active material consumption for the formation of the SEI film. From Fig. 4(a), the first semi-circle of the Nyquist plot represents the R_{sei}, and after 300 FEC, the emergence of a second semi-circle denotes the R_{sei} growth, which is also compatible with the fitting outcomes in Fig. 4(h). The SEI layer is continuously formed, shed, and precipitated in all the instances, which causes an increase in interface impedance and the rising trend in the R_{sei}. In Fig. 4(i), the R_{ct} development can be linked to an increase of electrode cracks, which lowered the conductivity of the fully charged batteries. It is important to note that the cells aged under 1 C and 2 C CCCV charge protocols had a significantly larger increase in R_{ct} as compared to MCCCV2. It was also demonstrated that a higher charging current is responsible for a rapid capacity decrease after 200 FEC since the faster charging in the high SOC range damages the electrode structure.

In summary, electrode degradation accelerates when high charging current is applied at high SOC. Therefore, avoiding large currents at high SOC helps to increase the lifetime of Li-ion batteries. The proposed multi-step fast-charging approach, which was developed based on the performance of graphite coin cells, has demonstrated its efficacy and efficiency for NMC cylindrical cells as well. The results from the IC suggest that the capacity fade is due to the loss of active materials and damage to the negative electrodes, while EIS results indicate that an increase in the charge transfer resistance is the main contribution to the overall increase in internal resistance. Compared to the degradation levels of standard CCCV charging protocols, the designed MCCCV2 method can extended the battery lifetime by additional 200 FEC before reaching 10% capacity fade. This is due to the slowing down of the SEI layer growth and R_{ct} increase as well as due to reduced electrode degradation. To further confirm this conclusions, post-mortem analysis was carried.

4. Post-mortem analysis of the electrodes

To further investigate the degradation mechanisms, the morphology of the electrodes was studied by SEM, as shown in Fig. 5. Fig. 5(a–h) display the SEM results for the cathodes corresponding to the cells aged under 1 C, 2 C, MCCCV1, and MCCCV2 charging conditions, while the results for the anodes are presented in Fig. 5(i–p). The cathodes are secondary particles, which consist of a large number of primary cubic grains with a size of 1–2 μm. In Fig. 5(f and g), the active materials were observed as dispersed grains, which indicates that their structure was damaged by high currents applied in the initial and final stages of the charging process. When Li ions are inserted and extracted fast, the mechanical stress damages the active materials leading to the formation of secondary particles, and, thus resulting in R_{ct} increase. The gaps between large agglomerates of cathode materials are due to the loss of binder materials, which is also observed in the disassembled process shown in Fig. S2. Thus, the charge resistance is increased due to the loss of conductivity of cathode active materials. Among all the four different test cases, the MCCV2 cathode exhibits the most similar morphology to the fresh cathode, which is shown in Fig. S3; This observation indicates that in the initial 20% of SOC, fast de-lithiation has significantly less negative impact than between 20% and 40%; however, when the battery is close to fully charged condition, the binder around the cathode active materials is destroyed by fast de-lithiation.

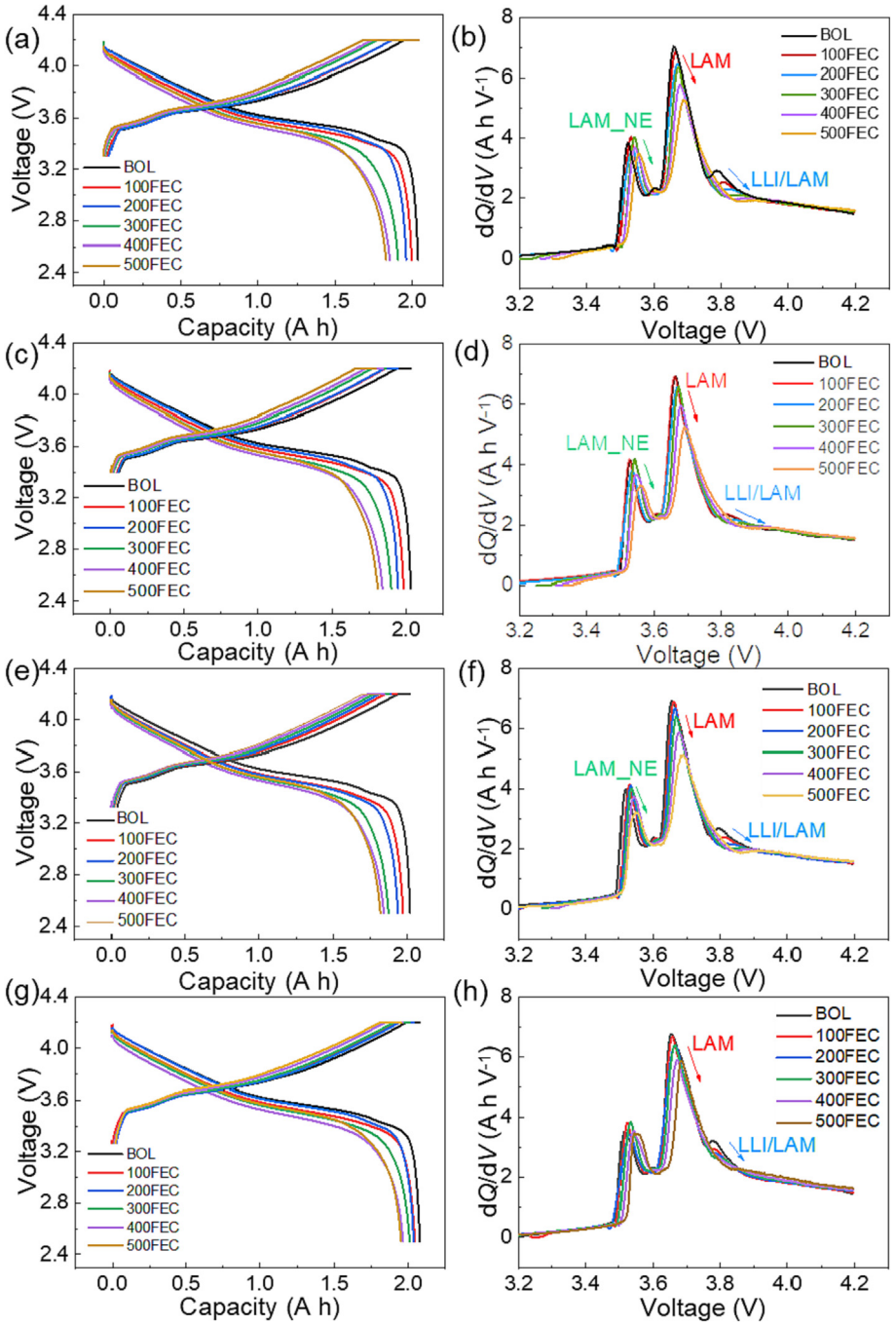

Fig. 3. Charge-discharge curves of acquired after every 100 FEC for four test cases of 18,650 NMC/graphite cells under different charging protocols: (a, b) 1 C, (c, d) 2 C, (e, f) MCCCV1, (g, h) MCCCV2. LAM: loss of active materials; LAM_NE: loss of active materials on negative electrode; LLI: loss of lithium inventory.

To further investigate the difference between 0–20% SOC and 20%–40% SOC, coin cells have been employed to aging under different SOC. Four coin cells and aging under 0–20% and 20%–40% SOC separately, and the morphology of electrodes are provided as Fig. 6. From the results observed from the SEM images, after cycling between 0–20% and 20%–40% SOC for several cycles, the morphology exhibited a large difference. After cycling between the 20% and 40% SOC, the cathode materials were observed dispersed grains, meanwhile the cathode cycled between 0% and 20% is similar to the fresh one. It is demonstrated that when Li ions are inserted and extracted fast after the initial 20% SOC, the mechanical stress damages the active materials leading to the formation of secondary particles, and, thus resulting in R_{ct} increase. From the cycled anode, more graphite exfoliation also appeared in the 20%–40% SOC range, considering the XRD results in Fig. 1(c), when the lithium ion inserted into graphite, the crystallization will change during the process. Higher current will lead to the large mechanical stress, which could cause the broken of the anode as well as the loss of active materials. In summary, the charging current applied in 20%–40% SOC leading to the significant SOH difference between MCCCV1 and MCCCV2.

Understanding the aging mechanisms of the graphite anode has been always an issue because of its unpredictable behavior. The defects and exfoliation on the aged anode surfaces are highlighted with red circles. The anode aged according MCCCV2 protocol has a smoother surface in general, while anodes aged in three other pro-

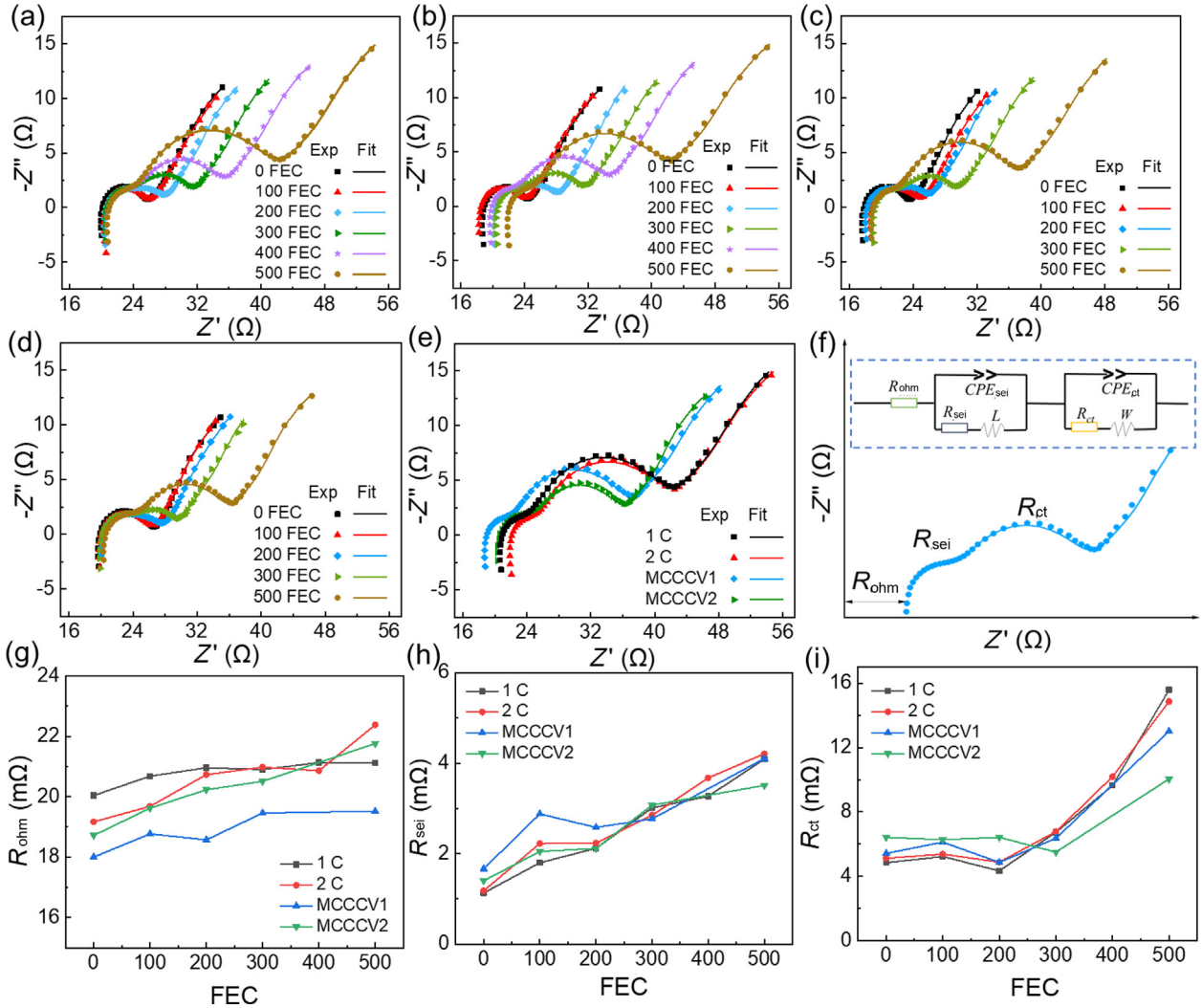

Fig. 4. EIS spectra of 18,650 NMC/graphite cells subjected to four different charging protocols. Spectra were acquired after every 100 FEC and fitted to an equivalent circuit model: (a) 1 C, (b) 2 C, (c) MCCCV1, (d) MCCCV2, (e) comparison of the four conditions at 500 FEC, and (f) equivalent circuit model; fitting resistance data of (g) R_{ohm}, (h) R_{sei}, (i) R_{ct}.

tocols show more cracks, leading to the loss of active material and a decrease in the charge transfer rate (an increase in R_{ct}). Nevertheless, the degradation was difficult to be quantitatively quantified through morphological analysis. Therefore, structural characterizations have been applied to quantify the defects of aged anodes.

Raman spectroscopy is used as a precise tool to characterize the defects of the graphite surface. As shown in Fig. 7(a), three peaks in Raman spectra of anodes can be identified: D peak, G peak, and G' peak, located at around 1400, 1600, and 2700 cm^{-1}. The value of I_D/I_G intensity ratio is associated with the amount of defects in graphite, the larger the ratio, the more defects the graphite contains [33]. For the fresh anode, I_D/I_G was 0.046, which is quite close to 0, indicating good crystallinity. As expected, MCCV2-aged anode demonstrated the lowest I_D/I_G of 0.27 as compared to the other three aged anodes, which showed 0.30, 0.32, and 0.29 for 1 C, 2 C, and MCCCV1 aging protocols, respectively. This verifies the conjecture based on the SEM morphology and fits well with the reality of the capacity degradation. The structure damage to electrodes from the applied high current during the initial stage of charge is extremely limited. This was also proved in the X-ray diffraction (XRD) patterns in Fig. 7(b). Evident graphite characteristic peaks can be seen in all XRD patterns at 27°. It is worth mentioning that the intensity ratio of the (010) and (004) peaks varies for different charging protocols. The anode from the MCCCV2 aging test retained the same peak ratio as the fresh anode, contrary to the anodes corresponding to the three other aging protocols. This indicates that the crystallinity of graphite was affected by high currents at 20%–40% and higher SOC stages, so (004) plane became the more common crystalline plane instead of (010) [34,35]. Similar to the fresh anode, all four aged anodes show diffraction peaks with good crystallinity at the end of the cycling process, which also points to the high structure stability of the graphite anode. The XRD patterns for the cathodes are shown in Fig. 7(c). Compared to the anodes, the cathodes corresponding to four different aging protocols show only minor difference, indicating a much less impact of current on the crystallization of cathode materials. Meanwhile, according to the data-driven cathode research, X-ray techniques with machine learning can be used as a powerful tool for uncovering the lattice structure in battery cathodes [36]. The structure stability, especially the thermal stability, is an essential factor for battery stability performance. The differential scanning calorimetry (DSC) curves for the four aged anodes are plotted in Fig. 7(d). Two obvious main exothermic peaks of decomposition occurred at 312.9 °C for the 2 C-aged anode and 310 °C for MCCCV1-aged anode, while for the 1 C-aged anode, a very broad peak was observed in the

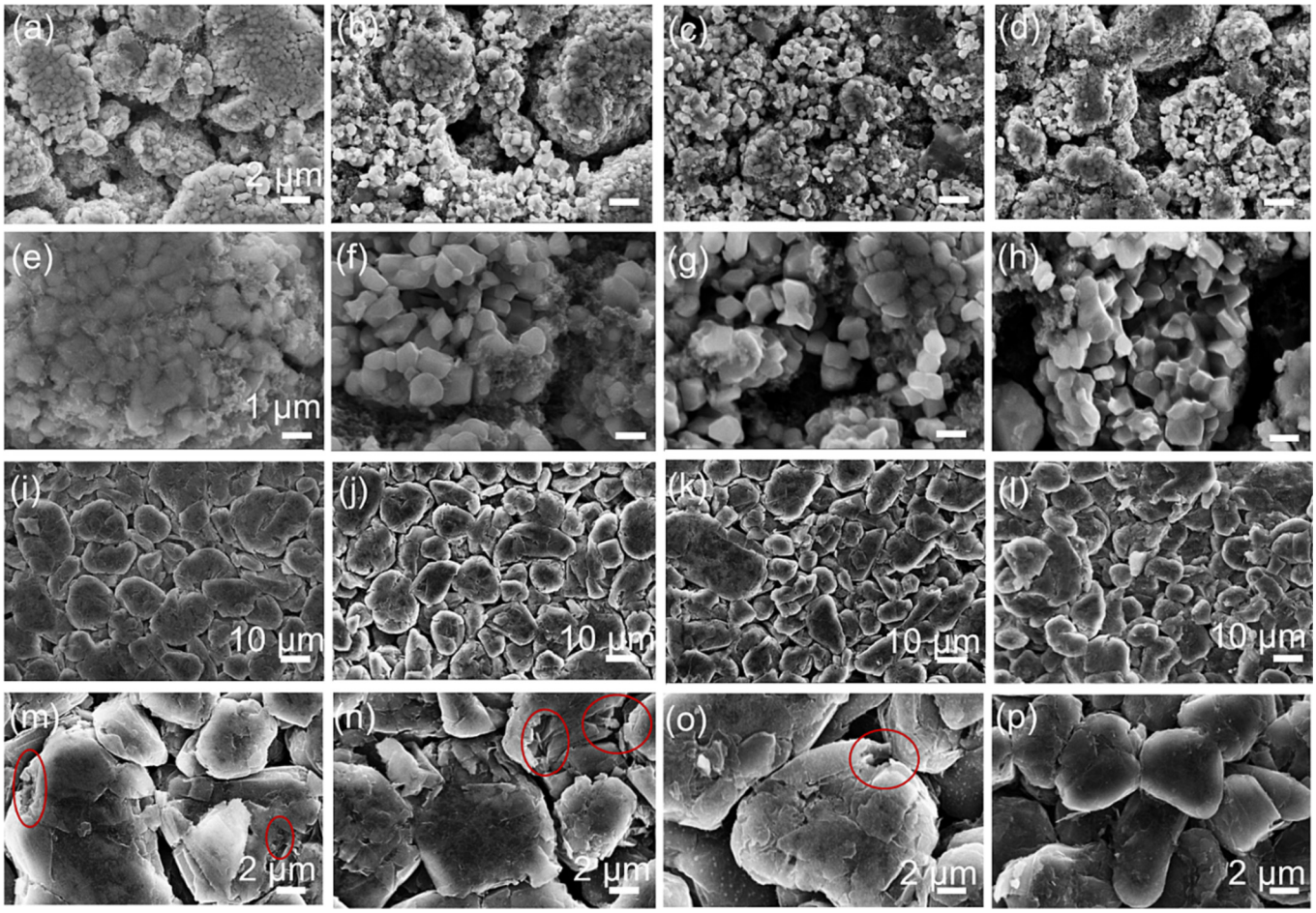

Fig. 5. Morphology images of aged NMC cathodes from 18,650 cells subjected to four different charging protocols (a, e) 1 C, (b, f) 2 C, (c, g) MCCCV1 and (d, h) MCCCV2, and the respective anodes images for (i, m) 1 C, (j, n) 2 C, (k, o) MCCCV1 and (l, p) MCCCV2 charging protocols. The red circles are highlighting the defects and exfoliation on the anode.

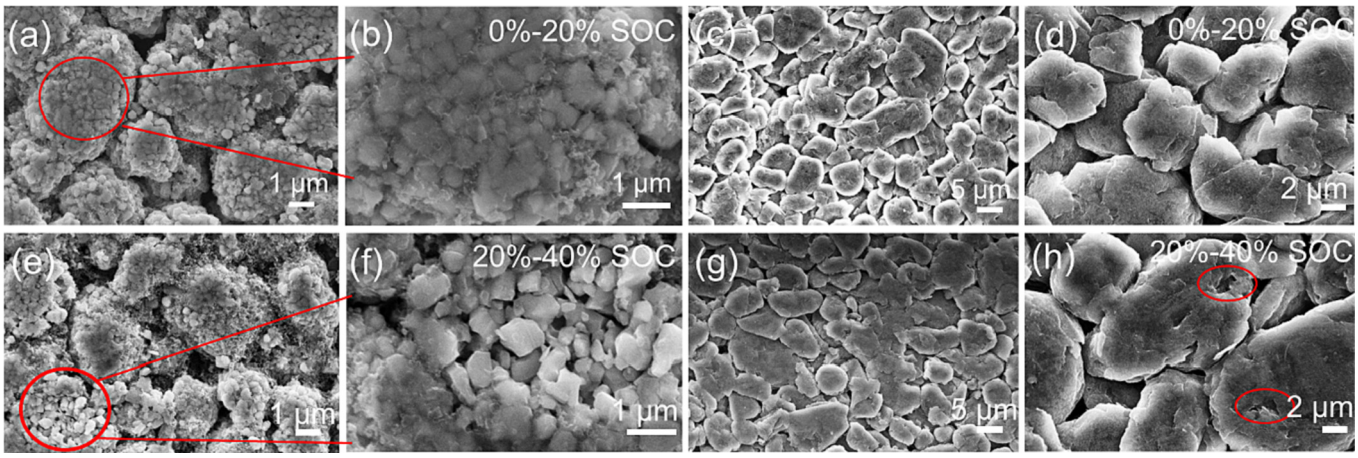

Fig. 6. Morphology images of cycled electrodes between 0–20% SOC (top) and 20%–40% (bottom): (a, b) aged cathode and anode (c, d) between 0–20% SOC; (e, f) aged cathode and anode (g, h) between 20%–40% SOC.

same range. In contrast, the MCCCV2 aged anode exhibited a smooth curve similar to the fresh anode, which implies that the thermal properties of MCCCV2 aged anode still remains relatively stable after long-term cycling [37]. The result demonstrates that low current applied at the end of the charging process can reduce the damage to the structure and maintain the thermal stability of graphite anode effectively.

Besides the structural defect on the electrodes, loss of active materials and formation of SEI layers are also a critical factor influencing the lifetime of Li-ion batteries. To quantify the elemental

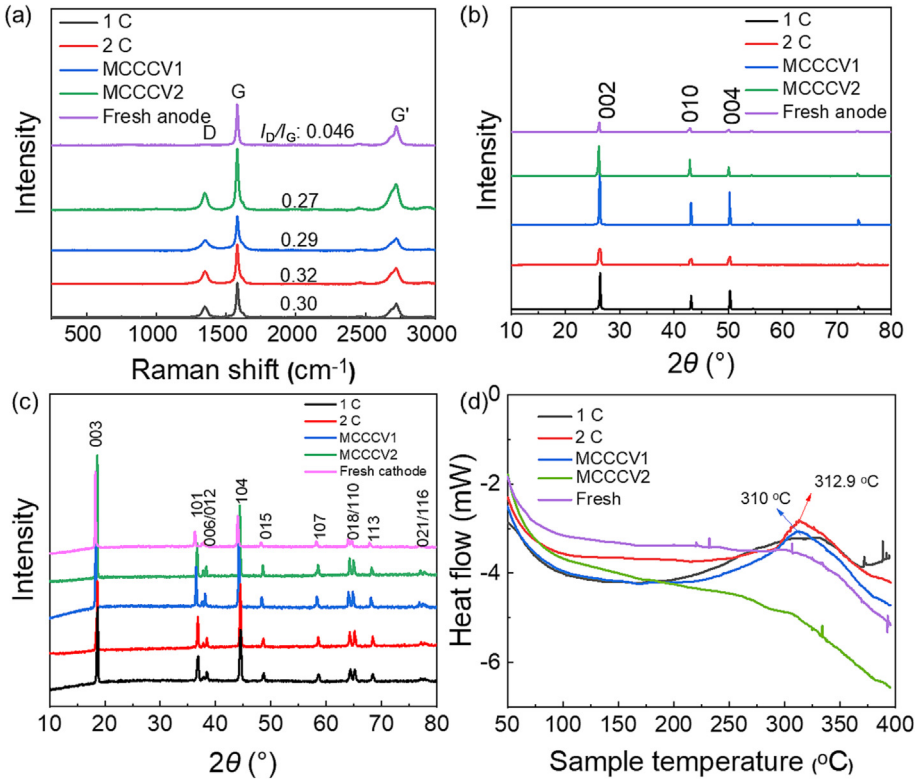

Fig. 7. Structural analysis of aged electrodes from 18,650 cells: (a) Raman spectrum, (b) XRD pattern of anodes, (c) XRD pattern of cathodes, and (d) DSC analysis of anodes.

composition on the electrodes, after 10% capacity fade, X-ray photoelectron spectroscope is applied to characterize the surface of the opened electrodes. Fig. 8 shows the XPS spectra corresponding to the MCCCV2 (Fig. 8a–c) and standard 1 C CCCV (Fig. 8d–f) charging. Four peaks are seen in the C 1*s* spectrum: the single bond peaks at 284.8 eV (C—H) and at 285.6–286.3 eV (C—O), the double bond peak at 288.7–288.8 eV (C=O), and the peak at 289.9–290.0 eV corresponding to O–C=O group (Li_2CO_3) [38,39]. The typical functional groups can be identified according to the C 1 *s* spectrum in Fig. 8(a and c). The relative peak area of Li_2CO_3, which is the primary component of SEI film, exhibits a modest rise (9.13%–9.60%) from MCCCV2 method to the standard 1 C CCCV method, as can be observed from the XPS spectra [32]. This suggests that rapid charging in the initial stage will not increase the amount of electrolyte degradation products that deposit on graphite's surface. In contrast, the higher current at the end of the charging process is more likely to generate SEI. The F 1*s* spectrum displays two prominent peaks that are attributed to LiF (684.8–684.9 eV) and $Li_xPO_yF_z$ (686.7–686.9 eV) [39,40]. The F 1*s* spectrum reveals that at standard charging protocols, more LiF is generated while at the same time, less $Li_xPO_yF_z$ is present. The increase in the LiF primarily reflects the decomposition of $LiPF_6$ salt in the electrolyte [41].

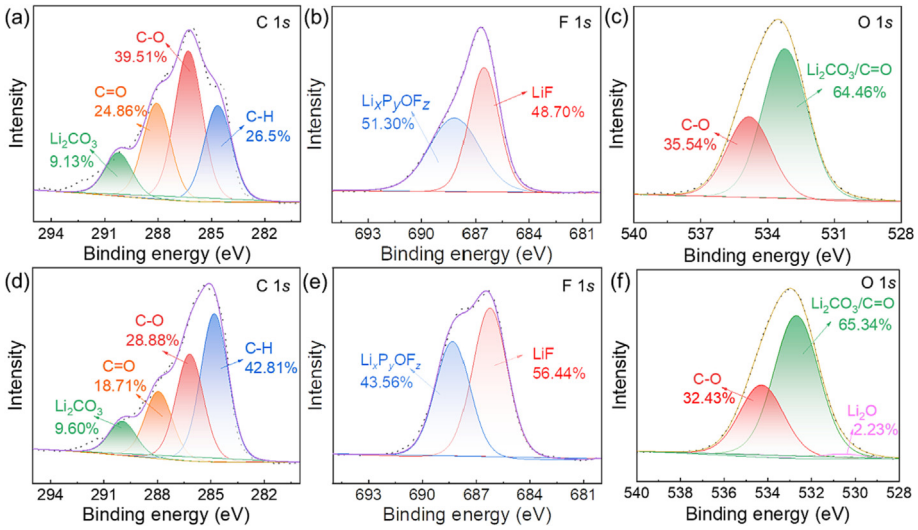

Fig. 8. XPS spectra in C 1*s*, F 1*s* and O 1*s* spectral ranges for graphite anode surfaces aged from 18,650 cells according (a–c) MCCCV2 and (d–f) standard 1 C CCCV charging protocol. The contributions of the specific peaks are marked.

Table 2
Summary of diagnostic methods and the corresponding results.

Diagnosis method		Results
Non-destructive		
	Capacity	MCCCV2 exhibits the largest capacity (94% SOH) at 500 FEC comparing to the other three reached 90% SOH.
	IC	MCCCV2 protocol shows the least increase in internal resistance, as well as the minimal loss of active materials.
EIS	The internal	resistance (both R_{sei} and R_{ct}) of MCCCV2 exhibits the slightest increase compared to other protocols.
Destructive	SEM	The anode morphology of MCCCV2 shows the smoothest surface which indicates less exfoliation as well as reduced R_{ct} on the anode; MCCCV2 cathode exhibits the most similar morphology to the fresh cathode, the secondary particles are not damaged by the de-/lithiation.
	XRD	The crystallization condition of MCCCV2 is closest to the fresh anode. The lattice in the first 20% SOC conditions has not changed comparing to the d-spacing increase when the SOC higher than 20%, which means the high current in the SOC higher than 20% will increase mechanical stress and lead to the damage of the graphite layer.
	XPS	The lower composition of the SEI layers on MCCCV2 anode implies that the reduced SEI layer growth on anode to decrease the resistance of R_{sei} and extend the lifetime.
	Raman	MCCV2-aged anode demonstrated the lowest I_D/I_G of 0.27 as compared to the other three aged anodes, which indicates that the least defects on the anode after aging.
	DSC	MCCCV2-aged anode exhibited a smooth curve similar to the fresh anode, which implies that the thermal properties of MCCCV2-aged anode still remain relatively stable after long-term cycling.

The CCCV-charged anode appears to have more Li_2CO_3/C═O (531.7–531.8 eV) than C—O (533.2–533.7 eV) in the O 1*s* spectra. The findings from O 1*s* spectra are consistent with the rise in Li_2CO_3 in C 1*s* spectra, which implies Li_2CO_3 gets deposited on the anode surface during high charging rate cycling at the high SOC [42]. Furthermore, the existence of Li_2O in O 1*s* of CCCV cases may be explained by the Li_2CO_3 decomposition under a high charge current when the battery reaches high SOC. In other words, high current charging causes the decomposition of solvents and $LiPF_6$ salt, which increases the amount of LiF, Li_2CO_3, and Li_2O on the surface of the graphite. As the result, a high current applied at high SOC accelerates the growth of the SEI layer on the anode, representing the increase of R_{sei}, which leads to the faster capacity drop of the full cells.

Overall, the loss of active materials for both anode and cathode under charging/discharging cycles is observed in SEM images, while the increase in the resistance (R_{ct} and R_{sei}) is explained by the observed structure and composition changes of SEI layers from Raman, XRD, DSC, and XPS. Based on the results above, it is explained that the cell aged by the proposed MCCCV charging protocol exhibits less loss of materials as well as less increase in the resistance. Moreover, post-mortem analysis provides clear evidence about how the charging protocols affect the degradation of electrodes and reduce the lifetime of Li-ion batteries. Various characterization techniques of morphology, structure, and compositions of electrodes describe the aging mechanisms under different charging protocols, which summarized in Table 2, providing a better understanding of both macroscopic and microscopic changes occurring in Li-ion batteries.

5. Conclusions

In conclusion, it was found that high charging currents cause less damage to electrodes in the initial stage of the charging process. Based on this result, it was hypothesized that the cracking of the anode was related to the intercalation stages in the charging/discharging cycle and suggested that anode deterioration is the primary cause for the loss of capacity. To reduce the capacity fade while minimizing the charging time, a multi-step fast-charging methodology inspired by physical degradation mechanisms was presented. It was shown that this method extended the cycling lifetime by more than 200 FEC, as well as reduced the charging time. Experimentally, 18,650 NMC/graphite cells were charged using four different protocols until they lost 10% of their capacity. Afterwards their electrical performance was examined and post-mortem analysis was carried out on separate electrodes. High currents applied during the initial 20% of the charging process were found to unlikely cause anode exfoliation, while low currents used above 80% SOC helped to reduce the formation of gaps between active materials, binder, and current collector, as well as slowed down the formation of SEI layers on the anodes.

This work provides a thorough understanding of the aging mechanisms of Li-ion batteries under different charging protocols from both macroscopic and microscopic perspective, which may help in designing optimized charging protocols to improve the lifetime and efficiency of Li-ion batteries. It also clarifies how the structural changes of the graphite anode affect the battery performance and provides new ideas for synthesis and improvement of novel battery materials.

Declaration of competing interest

The authors declare that they have no known competing financial interests or personal relationships that could have appeared to influence the work reported in this paper.

Acknowledgments

The authors would like to thank the support from the China Scholarship Council (202006370035 and 202006220024) and the Otto Mønsted Fond (22-70-1620). Furthermore, the authors would like to thank Peter Kjær Kristensen for his help with XPS measurements, Donghong Yu for his help with XRD test, Lars Rosgaard Jensen for his help with Raman measurements, and Kim Houtved Jensen and Thomas Sørensen Quaade for helping with the experiment platform.

Appendix A. Supplementary data

Supplementary data to this article can be found online at https://doi.org/10.1016/j.jechem.2023.01.016.

References

[1] M. Weiss, R. Ruess, J. Kasnatscheew, Y. Levartovsky, N.R. Levy, P. Minnmann, L. Stolz, T. Waldmann, M. Wohlfahrt-Mehrens, D. Aurbach, M. Winter, Y. Ein-Eli, J. Janek, Adv. Energy Mater. 11 (2021) 2101126.
[2] W. Cai, Y.-X. Yao, G.-L. Zhu, C. Yan, L.-L. Jiang, C. He, J.-Q. Huang, Q. Zhang, Chem. Soc. Rev. 49 (2020) 3806–3833.
[3] Y. Li, J. Guo, K. Pedersen, L. Gurevich, D.-I. Stroe, Batteries 8 (2022).
[4] Y. Liu, Y. Zhu, Y. Cui, Nat. Energy 4 (2019) 540–550.
[5] X. Wu, Y. Bai, Z. Li, J. Liu, K. Zhao, Z. Du, J. Energy Chem. 56 (2021) 121–126.
[6] X. Zhu, H. Wang, S. Allu, Y. Gao, E. Cakmak, E.J. Hopkins, G.M. Veith, Z. Wang, J. Power Sources 465 (2020).
[7] M. Song, S.Y. Choe, J. Power Sources 436 (2019).

[8] J. Hu, F. Fan, Q. Zhang, S. Zhong, Q. Ma, J. Energy Chem. 67 (2022) 604–612.
[9] J. Liu, Q. Duan, M. Ma, C. Zhao, J. Sun, Q. Wang, J. Power Sources 445 (2020).
[10] J. Hu, S. Zhong, T. Yan, J. Power Sources 508 (2021).
[11] S.S. Zhang, J. Power Sources 161 (2006) 1385–1391.
[12] Z. Chu, X. Feng, L. Lu, J. Li, X. Han, M. Ouyang, Appl. Energy 204 (2017) 1240–1250.
[13] G.L. Zhu, C.Z. Zhao, J.Q. Huang, C. He, J. Zhang, S. Chen, L. Xu, H. Yuan, Q. Zhang, Small 15 (2019).
[14] D. Zhang, L. Li, W. Zhang, M. Cao, H. Qiu, X. Ji, Chin. Chem. Lett. 34 (2023).
[15] X. Han, T. Wu, L. Gu, M. Chen, J. Song, D. Tian, J. Chen, Chin. Chem. Lett. (2022).
[16] M. Xu, R. Wang, B. Reichman, X. Wang, J Energy Storage 20 (2018) 298–309.
[17] T.T. Vo, X. Chen, W. Shen, A. Kapoor, J. Power Sources 273 (2015) 413–422.
[18] M. Keyser, A. Pesaran, Q. Li, S. Santhanagopalan, K. Smith, E. Wood, S. Ahmed, I. Bloom, E. Dufek, M. Shirk, A. Meintz, C. Kreuzer, C. Michelbacher, A. Burnham, T. Stephens, J. Francfort, B. Carlson, J. Zhang, R. Vijayagopal, K. Hardy, F. Dias, M. Mohanpurkar, D. Scoffield, A.N. Jansen, T. Tanim, A. Markel, J. Power Sources 367 (2017) 228–236.
[19] J. Li, R.G. Landers, J. Park, J. Power Sources 456 (2020).
[20] T. Kenji, S. Venkat, J. Electrochem. Soc. 162 (2015) A635.
[21] M. Xu, X. Wang, L. Zhang, P. Zhao, Energy 227 (2021).
[22] Z. Du, D.L. Wood, I. Belharouak, Electrochem. Commun. 103 (2019) 109–113.
[23] X. Wu, L. Ma, J. Liu, K. Zhao, D.L. Wood, Z. Du, J. Power Sources 545 (2022).
[24] J. Guo, S. Jin, X. Sui, X. Huang, Y. Xu, Y. Li, P.K. Kristensen, D. Wang, K. Pedersen, L. Gurevich, D.-I. Stroe, J Mater Chem A Mater 11 (2023) 41–52.
[25] S. Barcellona, L. Piegari, J Energy Storage 29 (2020).
[26] S. Schweidler, L. de Biasi, A. Schiele, P. Hartmann, T. Brezesinski, J. Janek, J. Phys. Chem. C 122 (2018) 8829–8835.
[27] J.G. Qu, Z.Y. Jiang, J.F. Zhang, J Energy Storage 52 (2022).
[28] S. Jenu, A. Hentunen, J. Haavisto, M. Pihlatie, J Energy Storage 46 (2022).
[29] B. Ospina Agudelo, W. Zamboni, E. Monmasson, Energy 234 (2021).
[30] J. Guo, Y. Li, J. Meng, K. Pedersen, L. Gurevich, D.-I. Stroe, J. Energy Chem. 74 (2022) 34–44.
[31] W. Pan, X. Luo, M. Zhu, J. Ye, L. Gong, H. Qu, J Energy Storage 42 (2021).
[32] Q. Ma, Z. Chen, S. Zhong, J. Meng, F. Lai, Z. Li, C. Cheng, L. Zhang, T. Liu, Nano Energy 81 (2021).
[33] A. Guedes, B. Valentim, A.C. Prieto, S. Rodrigues, F. Noronha, Int. J. Coal Geol. 83 (2010) 415–422.
[34] N.C. Gallego, C.I. Contescu, H.M. Meyer, J.Y. Howe, R.A. Meisner, E.A. Payzant, M.J. Lance, S.Y. Yoon, M. Denlinger, D.L. Wood, Carbon N Y 72 (2014) 393–401.
[35] S. Schweidler, L. de Biasi, A. Schiele, P. Hartmann, T. Brezesinski, J. Rgen Janek, J. Phys. Chem. C 122 (2018) 8829–8835.
[36] Z. Xue, J. Li, P. Pianetta, Y. Liu, Acc Mater Res 3 (2022) 854–865.
[37] Y. Li, S. Deng, Y. Chen, J. Gao, J. Zhu, L. Xue, T. Lei, G. Cao, J. Guo, S. Wang, Electrochim. Acta 300 (2019) 26–35.
[38] X. Gao, H. Zhou, S. Li, S.L. Chang, Y. Lai, Z. Zhang, J. Colloid Interface Sci. 615 (2022) 141–150.
[39] S. Liu, L. Wang, C. Zhang, B. Chu, C. Wang, T. Huang, A. Yu, J. Power Sources 438 (2019).
[40] L. Lin, T. Liu, X. Bi, L. Tian, K. Yang, J. Liu, M. Li, Z. Chen, J. Lu, K. Amine, K. Xu, F. Pan, Nat. Nanotechnol. 14 (2019).
[41] V.A. Agubra, J.W. Fergus, J. Power Sources 268 (2014) 153–162.
[42] X. Liu, M. Gao, J. Zhao, X. Sun, Z. Li, Q. Li, L. Wang, J. Wang, W. Zhuang, J. Power Sources 495 (2021).